*Article*

# Anisotropic Magnetism in Gradient Porous Carbon Composite Aerogels

Jochen Bahner [1] , Nicolas Hug [1] and Sebastian Polarz [2],*

[1] Department of Chemistry, Universität Konstanz, Universitätsstrasse 10, 78547 Konstanz, Germany; jochen.bahner@uni-konstanz.de (J.B.); Nicolas.2.Hug@uni-konstanz.de (N.H.)
[2] Institute of Inorganic Chemistry, Leibniz-University Hannover, Callinstrasse 9, 30167 Hannover, Germany
* Correspondence: sebastian.polarz@aca.uni-hannover.de

**Abstract:** Porosity is of high importance for functional materials, as it allows for high surface areas and the accessibility of materials. While the fundamental interplay between different pore sizes and functionalities is quite well understood, few studies on gradually changing properties in a material exist. To date, only a few examples of such materials have been synthesized successfully. Herein, we present a facile method for synthesizing macroscopic carbon aerogels with locally changing pore sizes and functionalities. We used ultracentrifugation to fractionate differently functionalized and sized polystyrene nanoparticles. The assembly into gradient templates was conducted in a resorcinol–formaldehyde (RF) sol, which acted as a liquid phase and carbon precursor. We show that the modification of nanoparticles and a sol–gel precursor is a powerful tool for introducing dopants (sulfur and phosphorous) and metal nanoparticles (e.g., Ni) into gradient porous carbons formed during the carbonization of the RF sol. Understanding the underlying interactions between particles and precursors will lead to a plethora of possibilities in the material design of complex functionally graded materials. We showed this by exchanging parts of the template with magnetite–polystyrene composites as templating nanoparticles. This led to the incorporation of magnetite nanoparticles in the formed gradient porous carbon aerogels. Finally, gradually increasing concentrations of magnetite were obtained, ultimately leading to macroscopic carbon aerogels with locally changing magnetic properties, while the graded porosity was maintained.

**Keywords:** hierarchical porosity; aerogel; functional gradient material; graded porosity; composite materials; magnetism; carbon; magnetite

## 1. Introduction

Nature is the premier example of enhanced material properties in complex hierarchical structures where multiple separated functionalities act in synergy. The transfer of these concepts to synthetic material chemistry is highly researched and leads to enhanced properties, e.g., in energy technology [1–5]. Hierarchy in solids is mainly understood as the occurrence of structural elements with different dimensions in a single material. A prominent example is nanostructured carbon, where a combination of heteroatom doping, porosity and the introduction of metal(-oxide) nanoparticles leads to significantly improved performance when the materials are applied as electrodes for energy generation and conversion [6–8]. Further improvements are observable when these concepts are transferred to monoliths with macroscopic dimensions [9]. Furthermore, the usage of corresponding materials allows for an additional level of complexity. Instead of a statistical distribution of various functional properties, a graded transition between them can be implemented, resulting in so-called functional gradient materials (FGM) [10,11]. A relatively well-studied class of FGMs are materials exhibiting surface gradients. In this case, mostly thiols or silanes are used to modify gold or silicon surfaces [12]. A focus in this area of research is the creation of tailored hydrophilic/hydrophobic gradients influencing the wettability of the substrate to gain a local control over the contact angle [13]. Another possibility is the

modification of surfaces with nanoparticles, where external fields can be used to assemble them into gradient structures [14]. By contrast, examples of synthetic materials exhibiting graded 3D structures are less common, mainly due to a lack of established synthetic procedures. Progress in method development has been made using, for example, layer-by-layer casting [15], 3D printing [16], gradient density gelation [17] or structuration via external forces [18]. Especially, the field of materials exhibiting nanoparticle gradients is highly interesting, reasoned by the improved catalytic activity of composite materials [19,20]. Only a few possibilities capable of introducing directionality into such materials exist. Cölfen and co-workers investigated the sedimentation behavior of various nanoparticles, resulting in the synthesis of nanoparticle gradients in a gelatin matrix using ultracentrifugation [21]. In an impressive report, Niederberger et al. reported the first synthesis of porous materials exhibiting directionally changing magnetic properties. Synthesizing monolithic nanoparticle-based aerogels in external magnetic fields led to the introduction of locally changing concentrations of magnetite nanoparticles in a porous anatase matrix [18].

In the field of three-dimensional FGMs, materials exhibiting a graded porosity hold an important position. In addition to their enhanced mechanical stability and cell adhesion for biomedical applications [22], benefits have been reported in gas diffusion layers. This is attributed to the changing wettability, pore sizes and, therefore, diffusion properties along the gradient structure [23–25]. However, studies regarding porous FGMs are mostly of a theoretical nature, mainly due to the lack of established synthesis procedures [26]. The employed synthesis methods include, among others, anisotropic microphase separation [27], foam templating [28] and sintering–dissolution processes [29]. Among these methods, only a few allow for a precise control over the final pore sizes. Guzowski and co-workers recently published a remarkable study. Using highly flexible microfluidics, graded porous gelatin and hydroxyapatite monoliths with pore sizes ranging from 80 to 800 μm for potential applications in the field of biomimetics could be formed [30]. For smaller pore sizes, mainly polymeric membranes exhibiting graded porosity have been synthesized. This can be performed either postsynthetically by selective swelling approaches [31] or during synthesis by diffusion-controlled assembly processes [32]. Similar approaches can be transferred to fully inorganic materials, resulting in graded porous carbons after carbonization [27]. While a porosity gradient has been reported as beneficial, e.g., for electrodes [33–35], material development is hindered, as most examples only involve very large pores above 10 μm, and often, no controllable pore structure is obtainable. Furthermore, the synthesis of functionalized carbons and their composites exhibiting adjustable porosity gradients with pores smaller than 1 μm was not possible until now. As these materials are prominently discussed for next-generation electrode materials [19,20,36,37], the experimental validation of the theoretical studies remains difficult. Furthermore, gradient structures could improve various functional properties. It is also worth noting that the interplay between pore sizes and material properties is an important factor for various applications, e.g., the tailored modulation of the thermal conductivity and flexural strength in macroscopic materials [38]. These special thermal effects might be enhanced by a gradual change between the functional features. Special effects resulting from functional gradients are also expected in the field of electromagnetic interference shielding [39] and microwave adsorption [40], as the reflection and adsorption of electromagnetic waves is highly dependent on the local functional properties [41]. The wide field of possible applications makes the understanding of the formation mechanisms of FGMs highly interesting. A promising method for overcoming the shortage of suitable materials, finally allowing the creation of tailormade materials with graded functionalities, is gradient centrifugation [42].

We previously reported the synthesis of gradient porous carbon materials by fractionating mixtures of differently sized polystyrene spheres dispersed in resorcinol–formaldehyde in a preparative ultracentrifuge. The resulting materials showed promising direction-dependent properties when applied as electrodes in lithium–air batteries [43]. The method was further refined in a paper published in 2019, culminating in the generation of materials

exhibiting independent chemical and structural gradients [44]. Herein, we report the introduction of locally changing magnetic properties into gradient porous carbon materials. This seems promising due to potential synergistic effects in applications. Magnetic separation is already a powerful technique, which can be improved using ferromagnetic membranes to manage the retention of magnetic compounds [45,46]. Additionally, the enhancement of catalytic activity using magnetic fields is well studied [47], which can also be observed in carbon composite materials [48]. However, no investigations on the effects of locally graded functionalities and pore sizes in corresponding macroscopic materials exist to date, as their synthesis was not feasible until now.

## 2. Materials and Methods

### 2.1. Materials

Sodium styrene sulfonate (NaSS, >90%), sodium carbonate ($Na_2CO_3$, >99.8%), potassium persulfate (KPS, >99%), oleic acid (>90%), iron(III) chloride hexahydrate ($FeCl_3$, >97%), 2,4-dihydroxybenzaldehyde (>98%) and iron(II) chloride tetrahydrate ($FeCl_2$, >98%) were purchased from Sigma-Aldrich, St. Louis, MO, US. Sodium sulfite ($Na_2SO_3$, >97%), sodium bicarbonate ($NaHCO_3$, >99.7%), resorcinol (>99%) and styrene (>99%) were purchased from Merck KGaA, Darmstadt, Germany. Silver nitrate (>99.9%) was purchased from abcr, Karlsruhe, Germany. Aqueous formaldehyde solution (37 wt%) was purchased from Carl Roth, Karlsruhe, Germany. The styrene was distilled at 40 °C under reduced pressure before use, to remove the polymerization inhibitor; all the other chemicals were used as received. Deoxygenated Milli-Q-grade water was used for all the experiments.

### 2.2. Synthesis of Modification Agents

Poly(styrene-co-styrene sulfonate) (PSS) nanoparticles of various sizes were synthesized by emulsifier-free emulsion polymerization. Ag@PSS nanoparticles were synthesized by modifying the synthesized PSS particles by a surface-mediated reduction of silver nitrate to metallic silver. Both processes were performed as reported in our recent research [44]. After synthesis, the nanoparticle dispersions were purified by dialysis against water.

Synthesis of metal-salen complexes: Modified salen ligands of the chemical structure 4,4'-((1E,1'E)-(ethane-1,2-diylbis(azanylylidene))bis(methanylylidene))bis-(benzene-1,3-diol) were synthesized by the condensation of ethylenediamine and 2,4-dihydroxybenzaldehyde. The ligand was further reacted with metal acetates ($M(OAc)_2$ with $M^{2+}$ = Ni, Co or Mn), yielding the corresponding metal-salen complex. The synthesis was performed as previously reported [49].

Synthesis of Mag@PSS: Mag@PSS nanoparticles were prepared by a modification of a previously reported procedure [50]. First, magnetite nanoparticles where synthesized by precipitating $FeCl_2$ (60.3 mmol) and $FeCl_3$ (90.2 mmol) from aqueous solution (50 mL) by the addition of ammonium hydroxide (40 mL, 25 wt%) in the presence of oleic acid (17.9 mmol) at 70 °C. The resulting magnetite nanoparticles were recovered by centrifugation and washed three times with water. The remaining residue was dried under vacuum. The magnetite nanoparticles were converted into a water-stable ferrofluid by first dispersing the obtained residue (1 g) in heptane (6 g), followed by the addition of an aqueous SDS solution (0.1 M, 24 mL). After stirring for 1 h, the mixture was homogenized by ultrasonication (Bandelin Sonopuls TT13/FZ, 90% amplitude, 2 min) in an ice-cooled bath. The heptane was removed at 80 °C while stirring, resulting in a water-based magnetite dispersion. Magnetite–PSS nanocomposites (Mag@PSS) with low magnetite contents where then synthesized by emulsion polymerization. First, a styrene-in-water suspension was obtained by mixing an organic phase containing styrene (6 g) and hexadecane (0.25 g) with an aqueous SDS solution (0.1 M, 24 mL). After homogenization by ultrasonication (90% amplitude, 2 min) at 0 °C, a water-based magnetite dispersion (6 mL) was added, and the mixture was again homogenized by ultrasonication (50% amplitude, 1 min). The polymerization was initiated by the addition of KPS solution (5 mL, 14.8 mM) and a subsequent heating to 80 °C. After 30 min, acrylic acid (0.416 mmol, 30 mg) was added,

and the reaction was allowed to continue for 18 h. The resulting brownish dispersion was filtrated and, afterwards, purified by dialysis against water.

Synthesis of carbon materials: Resorcinol–formaldehyde (RF) sols were prepared by mixing resorcinol (3.77 g) with aqueous formaldehyde solution (37 wt%, 10 mL). The RF sol (1.8 mL) was mixed with binary polystyrene suspensions (1 mL total) and sodium bicarbonate solution (75 μL, 1.51 M). In the case of metal-doped carbon materials, solutions of salen complexes (200 μL, 0.15 M in dimethyl sulfoxide) were added. The resulting dispersion was transferred to a polyallomer (13 mm × 51 mm) centrifuge tube. PSS–RF composites were then prepared using a Beckman Optima L-70 ultracentrifuge (Beckman Instruments, Brea, CA, USA) with a swinging-bucket rotor (SW 55 Ti, Beckman Instruments) to maintain the centrifugal force parallel to the length of the tube. As the density of PSS is lower than the density of RF sols, all the PSS latex spheres floated to the top of the centrifuge tube, forming a packing of the PSS spheres, while RF filled the interstices between the PSS spheres. The centrifugation was performed at 40 °C and 20,000 to 30,000 rpm and typically lasted for 12 h to ensure the RF sol had gelled before removing the centrifugal force. The PSS–RF composite, which was located at the top of the sample, was then cut from the sample and aged in pressure-resistant laboratory bottles at 85 °C for three days, followed by drying at 85 °C for 1 day in a convection oven. Afterwards, the PSS–RF composite was calcined at 900 °C for 3 h (heating ramp, 5 °C min$^{-1}$) in a flow of $N_2$ to carbonize the RF polymer while the polystyrene template was concurrently removed.

### 2.3. Material Characterization

TEM: The samples for TEM analysis were prepared by drop casting diluted dispersions onto carbon-coated copper grids. After the evaporation of the solvent, HR-TEM images were acquired with a JEOL JEM 2200FS at an accelerating voltage of 200 kV.

SEM: For SEM imaging, monolithic carbon samples were cut into two pieces along the direction of the centrifugal force. Images were then acquired at several positions along the resulting cross-sections using a Zeiss field-emission (FE)–SEM Auriga Crossbeam operating at 3–15 kV. EDX data were recorded at the same positions using an Oxford Instruments X-Max 20 mm$^2$ Silicon Drift Detector mounted onto the microscope.

Further characterization: X-ray diffractions were performed with a Bruker AXS D8 Advance diffractometer using Cu-K$\alpha$ radiation. TGA measurements were performed using a Netzsch STA 429 F3 Jupiter. XPS measurements were performed by Tascon GmbH, Sulzbach, Germany. Superconducting quantum interference device (SQUID) measurements were performed using a Quantum Design MPMS-XL5 magnetometer.

### 3. Results and Discussion

Gaining a precise control over the porosity and functionality in carbon materials is a focus of current research, as enhanced properties in applications such as catalysis and separation seem likely. However, no possibilities for obtaining a precise control over the local environments of different functionalities in carbon materials have existed until now. We herein report a facile and highly flexible process using ultracentrifugation for making functionalized carbon materials, overcoming this scientific gap. The paper is structured as follows: first, we briefly describe the synthesis of homogenously modified carbons characterized by gradient porosity. Then, we report the first synthesis of magnetite–carbon composite materials (Mag@C) exhibiting combined porous and magnetic gradients. The final method is compatible with our developed doping methods leading to highly complex material architectures as shown in Scheme 1.
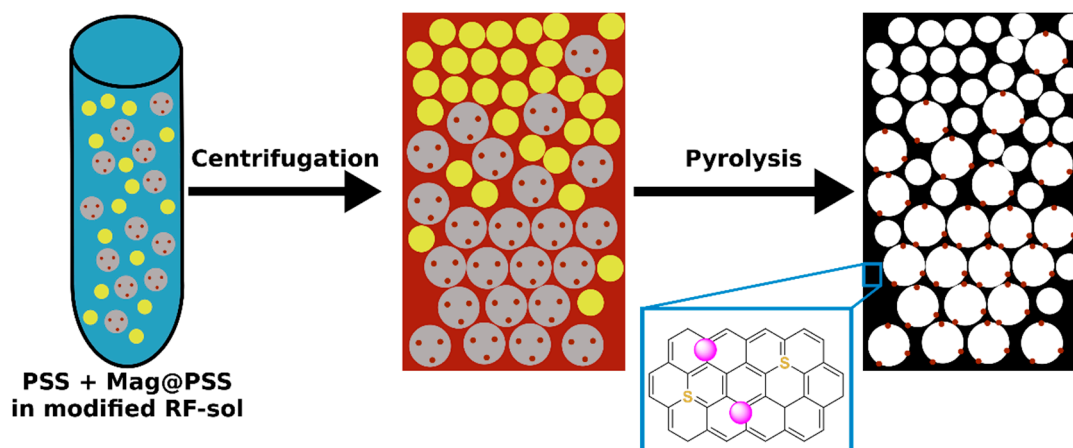
**Scheme 1.** Synthetic pathway for synthesizing gradient porous modified carbon aerogels with magnetic gradients. Yellow dots: poly(styrene-co-styrene sulfonate) (PSS) nanoparticles; brown dots: magnetite nanoparticles; gray/brown dots: Mag@PSS nanoparticles; magenta dots: metal (Ni, Co and Mn) nanoparticles.

### 3.1. Homogeneous Doping of Gradient Porous Carbons

The synthesis of gradient porous carbon materials with pore diameters between ~20 nm and ~1 μm can be realized using preparative ultracentrifugation (PUC) based on our previous reports [43,44]. Our process is based on the fractionation of differently sized polystyrene nanoparticles into templating structures characterized by gradually changing particle sizes. During centrifugation, an in situ infiltration with an RF sol, which gels during the centrifugation and fixes the gradient structure, is achieved. A following single pyrolysis step results in a concurrent carbonization and template removal. Importantly, this approach allows the introduction of different functionalities in the final carbon material through various pathways. First, we explored the introduction of a continuous modification over the entire gradient, realizing the decomposition of functionalized nanoparticles. The most basic material within our scope was synthesized by introducing a homogenous sulfur doping into the gradient porous carbon network. Therefore, we employed differently sized PSS nanoparticles acting as a template and doping agent simultaneously. The predicted continuous porosity gradient was maintained, as proven by scanning electron microscopy (SEM) micrographs taken along the direction of the centrifugal force (Supporting Information Figure S1). A sulfur doping was achieved during pyrolysis by the thermal decomposition of sodium styrene sulfonate to inorganic salts, which subsequently decomposed to sulfur oxides, acting as the doping agent [51]. The incorporation of sulfur into the material was confirmed using energy dispersive X-ray spectroscopy (EDX, Supporting Information Figure S2). X-ray photoelectron spectroscopy (XPS) further confirmed an incorporation of sulfur into the $sp^2$-hybridized carbon network. The main contribution in the S 2p region (Supporting Information Figure S3a) was detected at a binding energy of 164.5 eV, corresponding to C–S bonds, with only minor amounts of C–$SO_x$ species observable at 169.5 eV. In parallel, no significant S–O bonding was observed in the O 1s region (Supporting Information Figure S3b), confirming that the postulated doping from template decomposition was successful. Importantly, this process is easily transferable to other dopants such as phosphorous (P). A P-doping can be achieved by employing nanoparticles synthesized by the copolymerization of styrene and vinyl phosphonic acid as templates during synthesis (Supporting Information Figure S4).

### 3.2. Homogeneous Modification of Gradient Porous Carbon Composites

While the introduction of heteroatoms into gradient porous carbons by template decomposition works well, it is obviously limited by the need for heteroatom-containing monomers that can be polymerized into templating nanoparticles. As we aimed for the introduction of various potentially catalytically active modifications acting in synergy,

we investigated the synthesis of gradient porous carbon nanocomposites using modified precursors. We showed this by using hydroxyl-modified salen nickel complexes (see **5** in Supporting Information Scheme S1). The hydroxyl groups introduced into the complex underwent condensation, resulting in a binding to the RF sol during gelation [49], and were therefore incorporated in the carbon precursor gel, which was subsequently carbonized. We first showed the perseverance of the gradient porous structure by recording SEM micrographs at several positions along the cross-sections (Figure 1a) corresponding to the directions of the applied centrifugal force of the obtained macroscopic aerogels (Figure 1b).
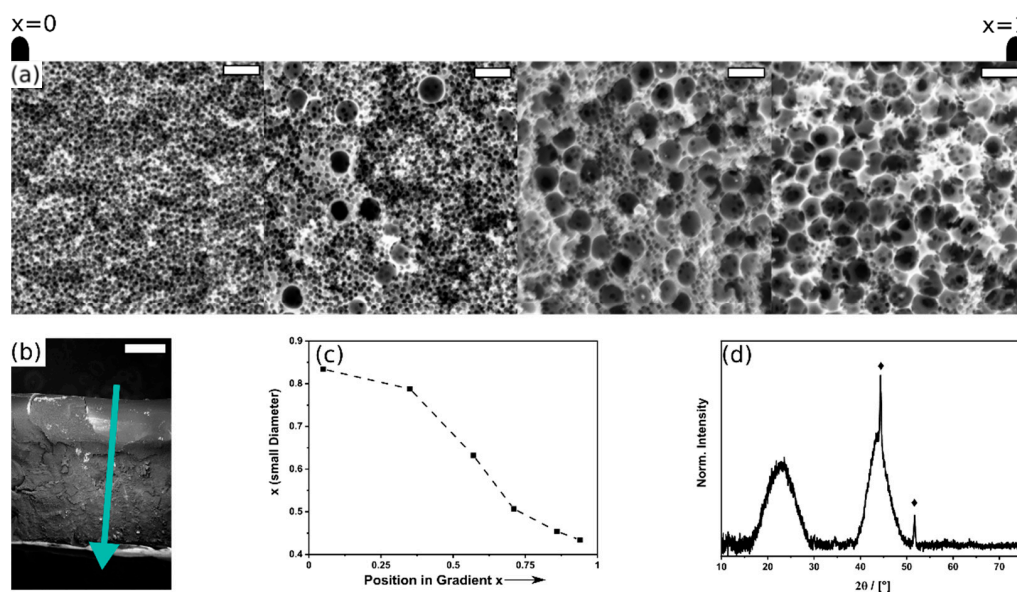


**Figure 1.** Ni@C material synthesized using PSS-137 and PSS-480 and a modified $Ni^{2+}$-salen complex. (**a**) SEM micrographs (scale bar: 500 nm) taken along the cross-section and (**b**) SEM micrograph of the cross-section (scale bar = 200 μm); arrow indicates the direction of the centrifugal force (start corresponds to x = 0; end, to x = 1). (**c**) Fraction of small pores along the gradient region as indicated in the cross-section determined by trainable Weka segmentation. (**d**) powder X-ray diffraction (PXRD) of a homogenized Ni@C sample, marked signals representing crystalline Ni.

The gradient porosity is clearly observable in the micrographs, as only small pores, templated by PSS-137, are visible at the beginning of the monolithic structure (x → 0), while the fraction of large pores, templated by PSS-480, increases towards the upper part of the monolith (x → 1). To verify that our introduced modifications did not influence the sedimentation behavior of the templating PSS nanoparticles, we evaluated the gradient region using machine learning provided by trainable Weka segmentation [52] implemented in ImageJ [53] as an objective parameter. As shown in Figure 1c, we calculated the local area fraction of small pores in dependence of the internal coordinate x. The correlation clearly shows a strong separation of the different pore sizes at the beginning and end of the gradient structure as previously reported [44]. At intermediate positions, a broad gradient region with both pore sizes and gradually increasing fractions of larger pores was formed. Besides the gradient formation, the incorporation of sulfur, resulting from the decomposition of the PSS, and nickel, formed by the decomposition of the modified salen complexes, could be observed by EDX (Figure S5). To clarify the structure of the Ni species, powder X-ray diffraction (PXRD, Figure 1d) of the composites was performed. In addition to the broad signals expected for turbostratic carbon at $2\theta = 23.3°$ and $2\theta = 43.9°$, additional reflexes from metallic nickel ($2\theta = 44.3°$ and $2\theta = 51.7°$) are clearly observable. This is in accordance with the bright structural features visible in the SEM micrographs (see Supporting Information Figure S6 for enlarged micrographs), which we attribute to nickel nanoparticles with diameters of ~30 nm. These are formed from molecular precursors by carbothermic reduction during carbonization. The broad applicability of our procedure

was further shown, as other metal nanoparticles could be introduced by utilizing salen complexes with other bivalent cations, as shown in Supporting Information Figure S7, for materials containing cobalt and manganese. The observed modification is promising for the synthesis of composite materials and highly suitable for modification with low levels of metal incorporation (the metal contents in the hybrid material are calculated to be 0.3–0.7 wt% according to EDX quantification), already leading to a high level of complexity.

### 3.3. Synthesis of Gradient Porous Magnetic Carbons

After showing the possibility of a homogenous modification of gradient porous carbon aerogels, we now focused on the synthesis of materials exhibiting dual gradients in magnetization and porosity. To achieve this, we identified Mag@PSS composite nanoparticles as a suitable template in the synthesis of gradient porous carbon materials. The successful encapsulation of small magnetite nanoparticles with diameters of 5 to 15 nm into the Mag@PSS template was confirmed by transmission electron microscopy (TEM), EDX linescan measurements, thermogravimetric analysis (TGA) and PXRD, all given in Supporting Information Figure S8. The magnetic properties of Mag@PSS were investigated using a superconducting quantum interference device (SQUID, Supporting Information Figure S9), confirming that the ferrimagnetism of the magnetite particles was retained in Mag@PSS nanoparticles, which were subsequently used in the synthesis of gradient porous carbon materials.

Carefully optimizing our synthetic procedure resulted in the formation of a magnetite/carbon composite, further denoted as Mag@C. During carbonization, the polystyrene portion of Mag@PSS decomposed, while magnetite nanoparticles remained bound to the pore walls of the final material. We first proved this using a polydisperse Mag@PSS sample as the template. As shown in Figure 2, the Mag@PSS/RF composite yielded after ultracentrifugation could be successfully converted to gradient porous magnetite–carbon composites, further denoted as Mag@C. Due to the, in this case beneficial, polydispersity of Mag@PSS, a gradient structure characterized by a smooth transition between pores from ~80 nm to ~5 μm was formed. The monolithic material (Figure 2a) was again investigated by SEM at distinct positions along the cross-section in the direction of the centrifugal force. At the start of the gradient region (Figure 2b), only small pores with an average diameter of 80 nm could be observed. The average diameter increased to 270 nm with a broad pore size distribution at intermediate positions (Figure 2c). As expected for a full fractionation of the polydisperse Mag@PSS sample, only very large pores with diameters between 1 and 5 μm were detectable at the end of the gradient area (Figure 2d), proving the formation of an extended gradient structure. The successful and homogeneous incorporation of magnetite and sulfur from the decomposition of the Mag@PSS nanoparticles was confirmed by EDX (Supporting Information Figure S10), supported by the visibility of magnetite nanoparticles as bright features in the SEM images (Figure 2b–d).
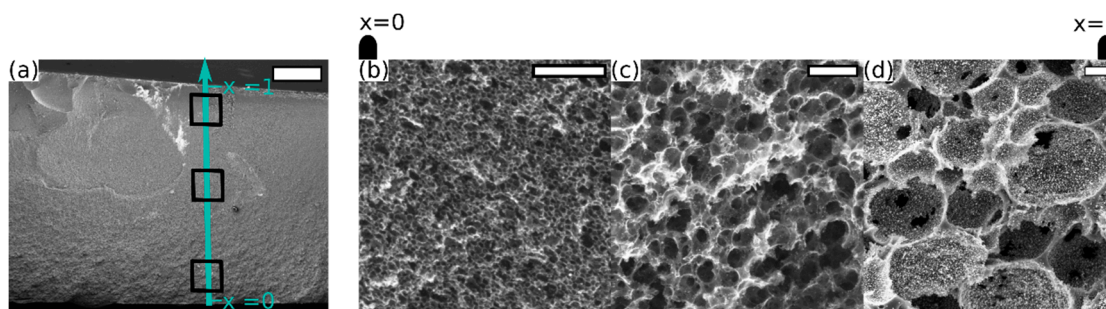


**Figure 2.** Analysis of a gradient porous Mag@C material by SEM. (**a**) SEM micrograph of the cross-section, showing the monolithic structure (scale bar: 200 μm), with rectangles indicating scanning positions, and arrow indicating direction of the centrifugal force with the internal coordinate x. (**b**–**d**) Enlarged SEM images (scale bar: 1000 nm) taken along the direction of the centrifugal force; positions according to the squares in (**a**).

A prerequisite for the aimed synthesis of carbons exhibiting gradually changing magnetic properties is the retention of the magnetism stemming from the magnetite nanoparticles. To investigate this, SQUID measurements (Figure 3) were performed on the templating Mag@PSS nanoparticles (blue curves) and the Mag@C composites (black curves). Measurements at 300 K (Figure 3a) revealed that both materials could be easily magnetized, exhibiting a quick equilibration magnetization as expected for ferrimagnetic materials. To clarify the origin of the magnetic properties, additional measurements were performed at 4 K (Figure 3b). The increase in saturation magnetization, as well as the formation of a hysteresis, observed for Mag@PSS and Mag@C is characteristic for materials exhibiting ferrimagnetic properties below the Curie temperature. As the shape of the hysteresis was similar, we conclude that the magnetite nanoparticles underwent no significant change in structure during template removal.
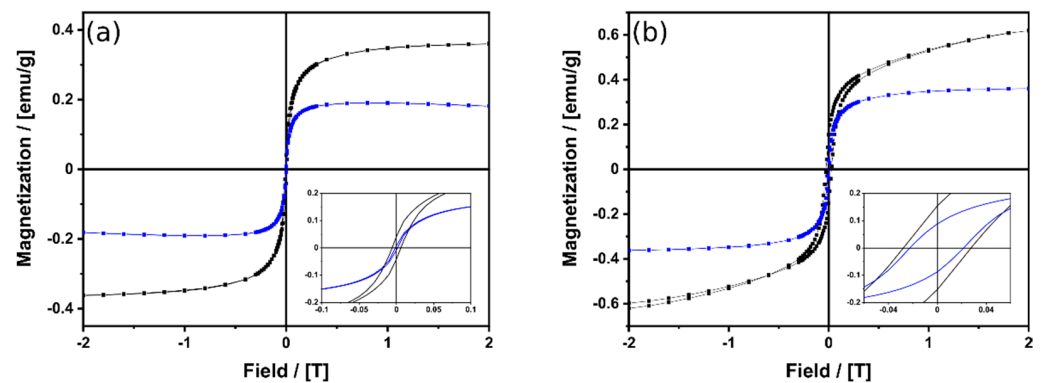


**Figure 3.** Superconducting quantum interference device (SQUID) measurement at (**a**) 300 K and (**b**) 4 K of Mag@PSS templates (blue curve) and the resulting gradient porous Mag@C material (black curve), with respective inlets showing the hysteresis region.

### 3.4. Synthesis of Carbons Exhibiting Gradient Porosity and Anisotropic Magnetization

Using the obtained knowledge, it was then straightforward to synthesize complex dual gradient materials as shown in Figure 4. Using mixtures of Mag@PSS and PSS-137 as templates, a gradual increasing magnetite content in the carbon material was expected, as magnetite was only incorporated at locations previously occupied by Mag@PSS. As these particles retain their magnetism, we proposed a resulting establishment of anisotropic magnetic properties. The resulting monoliths exhibit the expected structural gradient as revealed by SEM micrographs (Figure 4a) taken along the direction of the centrifugal force. At the start of the macroscopic gradient structure ($x \rightarrow 0$), only small pores, templated by the less dense and smaller PSS-137, were observed. The fraction of larger pores, templated by Mag@PSS, increased in the direction of the centrifugal force ($x \rightarrow 1$), showing the successful gradual separation of the templating nanoparticles. As the polydisperse Mag@PSS was further fractionated, the average pore size further increased along the gradient region, reaching a maximum at $x = 1$. The enlarged SEM images indicate the formation of an additional gradient characterized by a changing magnetite concentration. While no magnetite nanoparticles can be observed at $x \rightarrow 0$ (Figure 4b), bright features with diameters of 15 to 25 nm assignable to magnetite particles are clearly observable in regions with larger pores, as indicated by arrows in the inlets in Figure 4c. The incorporation of magnetite and sulfur into the material could be confirmed by EDX measurements (Supporting Information Figure S11) recorded along the direction of the centrifugal force. The increasing intensity of the iron signal clearly reveals an increasing magnetite content along the gradient of the centrifugal force coinciding with a constant sulfur doping homogenously detected at all the positions.
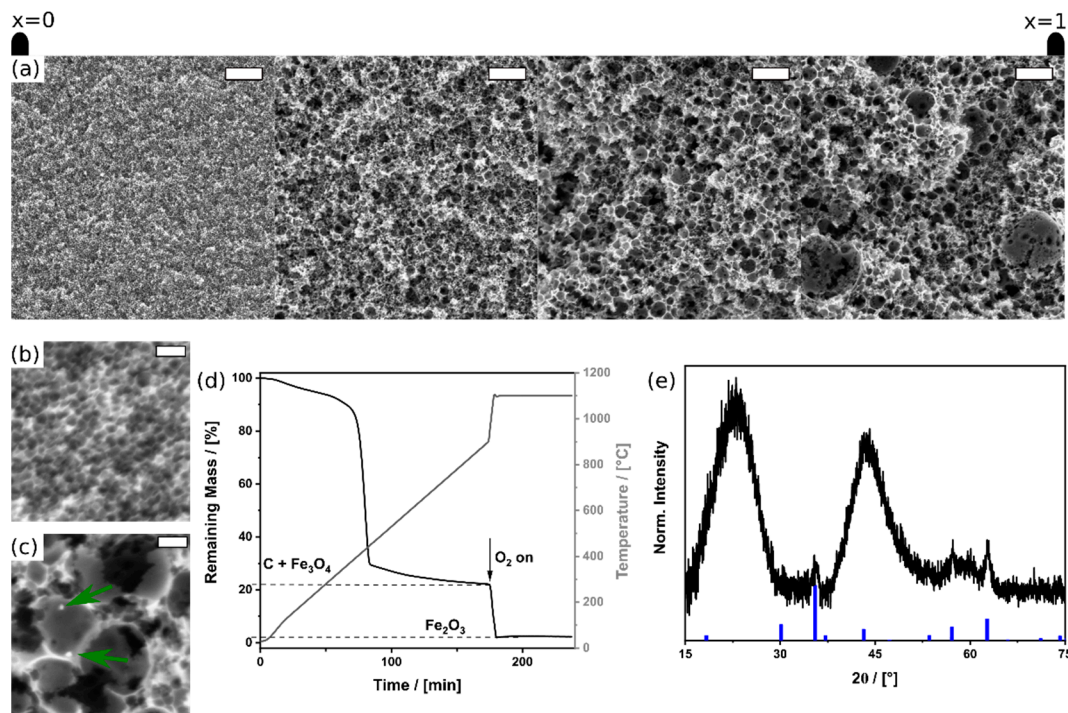
**Figure 4.** Analysis of a gradient porous Mag@C material with additional magnetite gradients. (**a**) SEM micrographs taken along the direction of the centrifugal force (scale bar: 1000 nm). Enlarged SEM micrographs (scale bar: 200 nm) at (**b**) x → 0 (left side of the gradient region) and (**c**) x → 1 (right side of the gradient region), arrows in (**c**) indicating magnetite nanoparticles. (**d**) TGA showing the carbonization process under nitrogen atmosphere and subsequent decomposition under oxygen atmosphere and isothermal conditions. TGA trace given in black, temperature given in gray. (**e**) PXRD measurements of homogenized Mag@C with magnetite reference (COD: 2101926) given in blue.

To clarify the formation mechanism for Mag@C, the thermal decomposition of an RF–Mag@PSS composite was investigated by TGA as shown in Figure 4d. Prominently, a sharp mass loss was detected between 350 and 400 °C under a nitrogen ($N_2$) atmosphere. This was caused by a rapid thermal depolymerization of the PaSS template, occurring concurrently with condensation reactions in the RF composite employed as the carbon precursor. The process culminated in a slow carbonization of the aged RF sol, indicated by the convergence towards a plateau at 900 °C, yielding gradient porous Mag@C materials. The magnetite concentration in the composite was determined by further heating under the addition of oxygen ($O_2$) to the atmosphere. This led to a complete decomposition of the carbon network after an isothermal treatment at 1100 °C with a residue of 2.3 wt%, formed by the oxidation of magnetite nanoparticles to hematite, remaining after the measurement. PXRD measurements (Figure 4e) of the material further confirmed the incorporation of magnetite particles into the final Mag@C materials. In addition to the expected broad reflexes for turbostratic carbon, broad reflexes assignable to crystalline magnetite were clearly visible as indicated by the blue bars in the diffractogram.

As a final step, we investigated the proposed magnetization gradient. To achieve this, the material was mechanically separated into two macroscopic pieces along the direction of the centrifugal force and analyzed using SQUID (Figure 5). One half corresponded to the low-magnetite side (x → 0, black curves), while the other half corresponded to the high-magnetite side (x → 1, blue curves). Measurements at 300 K (Figure 5a) revealed the retention of the magnetic properties under strong magnetic fields without significant hysteresis, as expected above the Curie temperature. Importantly, the observed saturation magnetization on the low-magnetite side (black curve) was smaller than on the higher-magnetite side (blue curve), indicating a gradually changing magnetization. The difference became more distinct below the Curie temperature at 4 K (Figure 5b), revealing a fourfold increased saturation magnetization at x → 1 in comparison to x → 0. The hysteresis

expected for ferrimagnetic materials was evident in both pieces. As the coercivity and shape of the hysteresis were constant in both pieces, we propose no change in the local chemical structure. However, the remanence was increased from 0.056 to 0.170 emu/g as expected for the proposed locally changing magnetizability in the carbon composites. The reason for this was the gradually increasing magnetite concentration in the graded porous sulfur-doped Mag@C, which is visualized in the red curves given in Figure 5a.
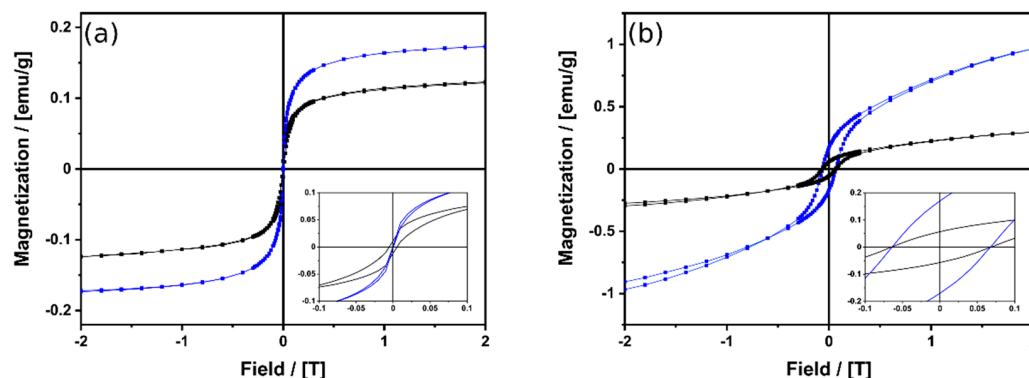


**Figure 5.** SQUID measurement at (**a**) 300 K and (**b**) 4 K on a mechanically separated sample at sides with high (blue curve) and low (black curve) magnetite concentrations, with respective inlets showing the hysteresis region.

### 3.5. Tailored Adjustment of Gradients and Functionalities

With the developed knowledge of the synthesis procedure, wide ranges of complex gradient materials are obtainable. For possible future applications, it will be important to control the pore sizes in the gradient region, as this would allow for a controlled modulation of the mass diffusion supported by the anisotropic magnetization. To achieve this, we showed the synthesis of dual gradient Mag@C materials (see Supporting Information Figure S12 for the SEM micrographs and EDX raw data) using differently sized PSS nanoparticles. Again, trainable Weka segmentation [52] was used to analyze the local fraction of the area composed of small pores templated by pure PSS particles, while the functional gradient was locally investigated using EDX. In all cases, a separation of PSS and Mag@PSS was achieved, resulting in the formation of a graded pore structure (dotted lines in Figure 6a). Accordingly, an additional functional gradient manifested in a gradually changing magnetite concentration (solid lines in Figure 6a) was realized, showing the flexibility of our method.

Besides the optimization of the gradient structure, the introduction of additional functionalities is promising, as their local environments can be customized. On the one hand, this can be achieved by introducing a homogeneous modification with metal nanoparticles, as the previously described addition of modified salen complexes during synthesis led to an incorporation of metallic nanoparticles into the Mag@C material (Supporting Information Figure S13). Beneficially, our approach offers an additional sophisticated method for synthesizing model systems for future investigations of synergistic effects in catalysis. Using Mag@PSS mixed with differently modified PSS particles as templates during synthesis leads to the introduction of other modifications. We demonstrated this by synthesizing gradient porous carbon nanocomposites templated by Mag@PSS and silver-modified PSS (Ag@PSS) nanoparticles. While a gradient porosity was maintained (Figure S14), the local concentrations of silver (dotted lines) and magnetite (solid lines) particles in the material could be precisely influenced as shown in Figure 5b. Depending on the diameters of the templating nanoparticles, either concurrent (orange curves) or separated (green curves) gradients could be achieved. PXRD (Supporting Information Figure S15) revealed the clearly distinguishable crystalline features from silver and magnetite, respectively. These materials could be employed as catalytically active membranes, combining the catalytic properties of silver/carbon composites [48] with a strong separation effect, caused by a

gradually changing magnetization [46] and anisotropic porosity. As the complexity of the herein-reported materials is unparalleled, the catalytic performance will have to be investigated in detail and will be subjected to further research.
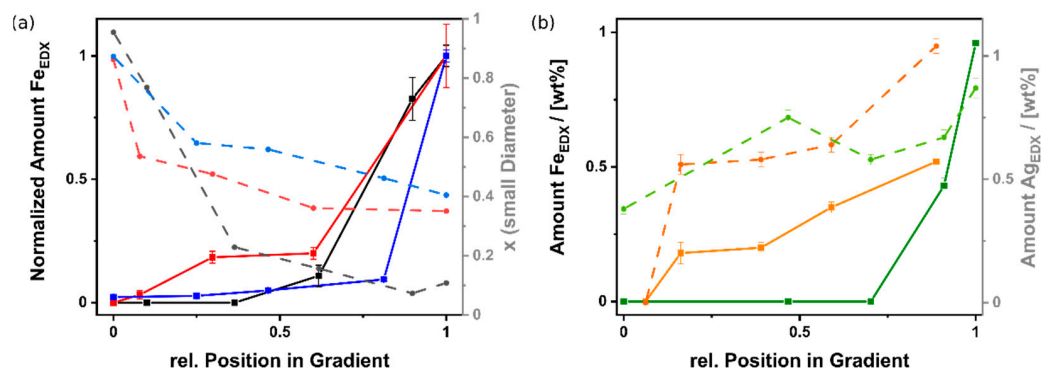


**Figure 6.** (**a**) Correlation of the Fe content (solid lines) and the area occupied by small pores (segmented lines) with the relative position in the gradient in various Mag@C. Black curves: combination of PSS-38 and Mag@PSS; red curves: combination of PSS-137 and Mag@PSS; blue curves: combination of PSS-288 and Mag@PSS. EDX spectra and SEM micrographs given in Figure S12. (**b**) Correlation of the Fe content (solid lines) and Ag content (segmented lines) determined by EDX with the relative position in the gradient in various Ag/Mag@C materials with different pore sizes. Green curves: Ag@PSS-480 + Mag@PSS; orange curves: Ag@PSS-138 + Mag@PSS. EDX spectra and SEM micrographs given in Figure S14.

## 4. Conclusions

Ultracentrifugation-guided templating is a powerful tool in the synthesis of complex gradient porous carbon materials. The introduction of various functionalities is possible by the careful adjustment of the synthesis process. While the decomposition of modified templating particles can lead to a heteroatom doping (S, P) of the carbon matrix, metal–carbon hybrids (Ni, Co and Mn) can be realized by the decomposition of metal complexes bound to the RF precursor by polycondensation during the formation process. As these additives do not alter the structuration of the materials, additional functional gradients can be introduced using hybrid Mag@PSS particles during the templating process. This results in materials exhibiting gradually changing magnetite concentrations in addition to pore size gradients ranging from 20 nm to 2 μm. An investigation of the magnetic properties showed that the local magnetization could be influenced using this approach. These complex architectures allow the generation of porous hybrids with highly controllable directional properties. Our introduced functionalities will allow for a broad range of possible applications, offering the possibility of performing detailed investigations, e.g., in magnetically enhanced catalysis and magnetic separation, in our future research. However, as the research on nanostructured gradient porous materials is only starting to attract interest, due to the to-date difficult and scarcely available synthesis methods, suitable test setups will have to be built up and validated first. Additionally, our method greatly enhances the range of material architectures of porous monolithic materials in contrast to classical approaches. As the possibility of locally optimizing the structural and chemical compositions of macroscopic aerogels could be transferred to other types of materials, timely realizable applications sparked by further research seem likely.

**Supplementary Materials:** The following are available online at https://www.mdpi.com/2311-5629/7/1/22/s1. Figure S1: SEM micrographs of a sulfur doped gradient carbon material, Figure S2: EDX measurement of a sulfur doped carbon material before and after washing, Figure S3: XPS spectra of a sulfur doped gradient porous carbon material, Figure S4: Analytic data of a phosphorous doped carbon material, Figure S5: EDX spectrum of a homogenized Ni@C sample, Figure S6: Enlarged SEM micrograph of a Ni@C sample, Figure S7 Metal-Carbon composites synthesized using 5, Figure S8: Analytical data of the synthesized MagPS nanoparticles, Figure S9: SQUID measurements of

magnetite particles and MagPS Particles, Figure S10: EDX spectra recorded along the direction of the centrifugal force of the material presented in Figure 2, Figure S11: EDX spectra of a material prepared using PSS-137 and Mag@PSS, Figure S12: Additional dual gradient materials, Figure S13: Analytical data for a material synthesized using PS-137, Mag@PSS and 5, Figure S14: Analytical data for Ag+Mag@C materials, Figure S15: PXRD of a dual gradient magnetite/silver material, Scheme S1: Synthesis of modified metal salen complexes.

**Author Contributions:** J.B. performed material preparation and analysis, and wrote the manuscript; N.H. contributed to the synthesis of the sulfur- and phosphorous-doped carbons; S.P. supervised the research and wrote the manuscript. All authors have read and agreed to the published version of the manuscript.

**Institutional Review Board Statement:** Not applicable.

**Informed Consent Statement:** Not applicable.

**Data Availability Statement:** The data created in this study are contained within the article and the corresponding supplementary material.

**Conflicts of Interest:** The authors declare no conflict of interest.

## References

1. Fratzl, P.; Weinkamer, R. Nature's hierarchical materials. *Prog. Mater. Sci.* **2007**, *52*, 1263–1334. [CrossRef]
2. Mann, S.; Ozin, G.A. Synthesis of inorganic materials with complex form. *Nat. Cell Biol.* **1996**, *382*, 313–318. [CrossRef]
3. Sun, M.-H.; Huang, S.-Z.; Chen, L.-H.; Li, Y.; Yang, X.-Y.; Yuan, Z.-Y.; Su, B.-L. Applications of hierarchically structured porous materials from energy storage and conversion, catalysis, photocatalysis, adsorption, separation, and sensing to biomedicine. *Chem. Soc. Rev.* **2016**, *45*, 3479–3563. [CrossRef]
4. Wegst, U.G.K.; Bai, H.; Saiz, E.; Tomsia, A.P.; Ritchie, R.O. Bioinspired structural materials. *Nat. Mater.* **2015**, *14*, 23–36. [CrossRef] [PubMed]
5. Xu, A.-W.; Ma, Y.; Cölfen, H. Biomimetic mineralization. *J. Mater. Chem.* **2006**, *17*, 415–449. [CrossRef]
6. Beda, A.; Villevieille, C.; Taberna, P.-L.; Simon, P.; Ghimbeu, C.M. Self-supported binder-free hard carbon electrodes for sodium-ion batteries: Insights into their sodium storage mechanisms. *J. Mater. Chem. A* **2020**, *8*, 5558–5571. [CrossRef]
7. Benzigar, M.R.; Talapaneni, S.N.; Joseph, S.; Ramadass, K.; Singh, G.; Scaranto, J.; Ravon, U.; Al-Bahily, K.; Vinu, A. Recent advances in functionalized micro and mesoporous carbon materials: Synthesis and applications. *Chem. Soc. Rev.* **2018**, *47*, 2680–2721. [CrossRef] [PubMed]
8. Zhou, M.; Wang, H.-L.; Guo, S. Towards high-efficiency nanoelectrocatalysts for oxygen reduction through engineering advanced carbon nanomaterials. *Chem. Soc. Rev.* **2016**, *45*, 1273–1307. [CrossRef]
9. Feinle, A.; Elsaesser, M.S.; Husing, N. Sol–gel synthesis of monolithic materials with hierarchical porosity. *Chem. Soc. Rev.* **2016**, *45*, 3377–3399. [CrossRef]
10. Rabin, B.; Shiota, I. Functionally gradient materials. *MRS Bull.* **1995**, *20*, 14–18. [CrossRef]
11. Khan, T.; Zhang, N.; Akram, A. State of the art review of functionally graded materials. In Proceedings of the 2019 2nd International Conference on Computing, Mathematics and Engineering Technologies (iCoMET), Sukkur, Pakistan, 30–31 January 2019; pp. 1–9.
12. Morgenthaler, S.; Zink, C.; Spencer, N.D. Surface-chemical and -morphological gradients. *Soft Matter* **2008**, *4*, 419–434. [CrossRef]
13. Wu, H.; Zhu, K.; Cao, B.; Zhang, Z.; Wu, B.; Liang, L.; Chai, G.; Liu, A. Smart design of wettability-patterned gradients on substrate-independent coated surfaces to control unidirectional spreading of droplets. *Soft Matter* **2017**, *13*, 2995–3002. [CrossRef] [PubMed]
14. Nardi, T.; Leterrier, Y.; Karimi, A.; Månson, J.-A.E. A novel synthetic strategy for bioinspired functionally graded nanocomposites employing magnetic field gradients. *RSC Adv.* **2014**, *4*, 7246–7255. [CrossRef]
15. Kim, J.; Nakanishi, H.; Pollanen, J.; Smoukov, S.; Halperin, W.P.; Grzybowski, B.A. Nanoparticle-loaded aerogels and layered aerogels cast from SOL-gel mixtures. *Small* **2011**, *7*, 2568–2572. [CrossRef] [PubMed]
16. Trachtenberg, J.E.; Placone, J.K.; Smith, B.T.; Fisher, J.P.; Mikos, A.G. Extrusion-based 3D printing of poly(propylene fumarate) scaffolds with hydroxyapatite gradients. *J. Biomater. Sci. Polym. Ed.* **2017**, *28*, 532–554. [CrossRef] [PubMed]

17. Gui, J.-Y.; Zhou, B.; Zhong, Y.-H.; Du, A.; Shen, J. Fabrication of gradient density SiO2 aerogel. *J. Sol-Gel Sci. Technol.* **2011**, *58*, 470–475. [CrossRef]

18. Heiligtag, F.J.; Leccardi, M.J.I.A.; Erdem, D.; Süess, M.J.; Niederberger, M. Anisotropically structured magnetic aerogel monoliths. *Nanoscale* **2014**, *6*, 13213–13221. [CrossRef] [PubMed]

19. Wu, G.; Santandreu, A.; Kellogg, W.; Gupta, S.; Ogoke, O.; Zhang, H.; Wang, H.-L.; Dai, L. Carbon nanocomposite catalysts for oxygen reduction and evolution reactions: From nitrogen doping to transition-metal addition. *Nano Energy* **2016**, *29*, 83–110. [CrossRef]

20. Cao, Y.; Mao, S.; Li, M.; Chen, Y.; Wang, Y. Metal/Porous Carbon composites for heterogeneous catalysis: Old catalysts with improved performance promoted by n-doping. *ACS Catal.* **2017**, *7*, 8090–8112. [CrossRef]

21. Spinnrock, A.; Schupp, D.; Cölfen, H. Nanoparticle gradient materials by centrifugation. *Small* **2018**, *14*, e1803518. [CrossRef] [PubMed]

22. Miao, X.; Sun, D. Graded/gradient porous biomaterials. *Materials* **2009**, *3*, 26–47. [CrossRef]

23. Zhan, Z.; Xiao, J.; Zhang, Y.; Pan, M.; Yuan, R. Gas diffusion through differently structured gas diffusion layers of PEM fuel cells. *Int. J. Hydrogen Energy* **2007**, *32*, 4443–4451. [CrossRef]

24. Omrani, R.; Shabani, B. Review of gas diffusion layer for proton exchange membrane-based technologies with a focus on unitised regenerative fuel cells. *Int. J. Hydrogen Energy* **2019**, *44*, 3834–3860. [CrossRef]

25. Ko, D.; Doh, S.; Park, H.S.; Kim, M.H. The effect of through plane pore gradient GDL on the water distribution of PEMFC. *Int. J. Hydrogen Energy* **2018**, *43*, 2369–2380. [CrossRef]

26. Stubenrauch, C.; Menner, A.; Bismarck, A.; Drenckhan, W. Emulsion and foam templating-promising routes to tailor-made porous polymers. *Angew. Chem. Int. Ed.* **2018**, *57*, 10024–10032. [CrossRef]

27. Hesse, S.A.; Werner, J.G.; Wiesner, U. One-pot synthesis of hierarchically macro- and mesoporous Carbon materials with graded porosity. *ACS Macro Lett.* **2015**, *4*, 477–482. [CrossRef]

28. Wang, C.; Li, J.; Guo, S. High-performance electromagnetic wave absorption by designing the multilayer graphene/thermoplastic polyurethane porous composites with gradient foam ratio structure. *Compos. Part A Appl. Sci. Manuf.* **2019**, *125*, 105522. [CrossRef]

29. Liu, C.; Liu, Y.; Liang, C.; Ma, Y.; Liu, W.; Yang, Y.; Cai, Q.; Tang, S. Novel approach for fabrication and characterisation of porosity-graded material. *Mater. Sci. Technol.* **2019**, *35*, 1583–1591. [CrossRef]

30. Costantini, M.; Jaroszewicz, J.; Kozoń, Ł.; Szlązak, K.; Święszkowski, W.; Garstecki, P.; Stubenrauch, C.; Barbetta, A.; Guzowski, J. 3D-printing of functionally graded porous materials using on-demand reconfigurable microfluidics. *Angew. Chem. Int. Ed.* **2019**, *58*, 7620–7625. [CrossRef] [PubMed]

31. Tan, D.; Li, Q.; Yang, B.; Wang, X.; Hu, S.; Wang, Z.; Lei, Y.; Xue, L. Continuous gradient nanoporous film enabled by delayed directional diffusion of solvent and selective swelling. *Langmuir* **2019**, *35*, 5864–5870. [CrossRef]

32. Cui, H.; Pan, N.; Fan, W.; Liu, C.; Li, Y.; Xia, Y.; Sui, K. Ultrafast fabrication of gradient nanoporous all-polysaccharide films as strong, superfast, and multiresponsive actuators. *Adv. Funct. Mater.* **2019**, *29*, 1807692. [CrossRef]

33. Liu, P.; Luo, Z.; Kong, J.; Yang, X.; Liu, Q.; Xu, H. Ba0.5Sr0.5Co0.8Fe0.2O3–based dual-gradient cathodes for solid oxide fuel cells. *Ceram. Int.* **2018**, *44*, 4516–4519. [CrossRef]

34. Gannon, P.; Sofie, S.; Deibert, M.; Smith, R.; Gorokhovsky, V. Thin film YSZ coatings on functionally graded freeze cast NiO/YSZ SOFC anode supports. *J. Appl. Electrochem.* **2008**, *39*, 497–502. [CrossRef]

35. Chen, L.; Yao, M.; Xia, C. Anode substrate with continuous porosity gradient for tubular solid oxide fuel cells. *Electrochem. Commun.* **2014**, *38*, 114–116. [CrossRef]

36. Lai, F.; Feng, J.; Heil, T.; Wang, G.-C.; Adler, P.; Antonietti, M.; Oschatz, M. Strong metal oxide-support interactions in carbon/hematite nanohybrids activate novel energy storage modes for ionic liquid-based supercapacitors. *Energy Storage Mater.* **2019**, *20*, 188–195. [CrossRef]

37. Hoffmann, C.; Thieme, S.; Brückner, J.; Oschatz, M.; Biemelt, T.; Mondin, G.; Althues, H.; Kaskel, S. Nanocasting hierarchical carbide-derived carbons in nanostructured opal assemblies for high-performance cathodes in lithium—Sulfur batteries. *ACS Nano* **2014**, *8*, 12130–12140. [CrossRef]

38. Han, M.; Yin, X.; Cheng, L.; Ren, S.; Li, Z. Effect of core-shell microspheres as pore-forming agent on the properties of porous alumina ceramics. *Mater. Des.* **2017**, *113*, 384–390. [CrossRef]

39. Han, M.; Yin, X.; Zhang, L.; Cheng, L.; Gogotsi, Y.; Hantanasirisakul, K.; Li, X.; Iqbal, A.; Hatter, C.B.; Anasori, B.; et al. Anisotropic MXene aerogels with a mechanically tunable ratio of electromagnetic wave reflection to absorption. *Adv. Opt. Mater.* **2019**, *7*, 1900267. [CrossRef]

40. Xu, H.; Yin, X.; Zhu, M.; Han, M.; Hou, Z.; Li, X.; Zhang, L.; Cheng, L. Carbon hollow microspheres with a designable mesoporous shell for high-performance electromagnetic wave absorption. *ACS Appl. Mater. Interfaces* **2017**, *9*, 6332–6341. [CrossRef] [PubMed]

41. Han, M.; Yin, X.; Hou, Z.; Song, C.; Li, X.; Zhang, L.; Cheng, L. Flexible and thermostable graphene/Sic nanowire foam composites with tunable electromagnetic wave absorption properties. *ACS Appl. Mater. Interfaces* **2017**, *9*, 11803–11810. [CrossRef]

42. Spinnrock, A.; Cölfen, H. Putting a new spin on it: Gradient centrifugation for analytical and preparative applications. *Chem. Eur. J.* **2019**, *25*, 10026–10032. [CrossRef]

43. Chen, M.; Hagedorn, K.; Cölfen, H.; Polarz, S. Functional gradient inverse opal Carbon monoliths with directional and multinary porosity. *Adv. Mater.* **2016**, *29*, 1603356. [CrossRef]

44. Bahner, J.; Klinkenberg, N.; Frisch, M.; Brauchle, L.; Polarz, S. Creating directionality in nanoporous carbon materials: Adjustable combinations of structural and chemical gradients. *Adv. Funct. Mater.* **2019**, *29*, 1904058. [CrossRef]

45. Yavuz, C.T.; Prakash, A.; Mayo, J.; Colvin, V.L. Magnetic separations: From steel plants to biotechnology. *Chem. Eng. Sci.* **2009**, *64*, 2510–2521. [CrossRef]

46. Podoynitsyn, S.N.; Sorokina, O.N.; Kovarski, A.L. High-gradient magnetic separation using ferromagnetic membrane. *J. Magn. Magn. Mater.* **2016**, *397*, 51–56. [CrossRef]

47. Steiner, U.E.; Ulrich, T. Magnetic field effects in chemical kinetics and related phenomena. *Chem. Rev.* **1989**, *89*, 51–147. [CrossRef]

48. Wang, H.; Shen, J.; Li, Y.; Wei, Z.; Cao, G.; Gai, Z.; Hong, K.; Banerjee, P.; Zhou, S. Porous carbon protected magnetite and silver hybrid nanoparticles: Morphological control, recyclable catalysts, and multicolor cell imaging. *ACS Appl. Mater. Interfaces* **2013**, *5*, 9446–9453. [CrossRef] [PubMed]

49. Kotbagi, T.V.; Shaughnessy, K.H.; LeDoux, C.; Cho, H.; Tay-Agbozo, S.; Van Zee, J.; Bakker, M.G. Copolymerization of transition metal salen complexes and conversion into metal nanoparticles supported on hierarchically porous carbon monoliths: A one pot synthesis. *J. Sol-Gel Sci. Technol.* **2017**, *84*, 258–273. [CrossRef]

50. Ramírez, L.P.; Landfester, K. Magnetic polystyrene nanoparticles with a high magnetite content obtained by miniemulsion processes. *Macromol. Chem. Phys.* **2003**, *204*, 22–31. [CrossRef]

51. Yao, Q.A.; Wilkie, C. Thermal degradation of blends of polystyrene and poly(sodium 4-styrenesulfonate) and the copolymer, poly(styrene-co-sodium 4-styrenesulfonate). *Polym. Degrad. Stab.* **1999**, *66*, 379–384. [CrossRef]

52. Arganda-Carreras, I.; Kaynig, V.; Rueden, C.; Eliceiri, K.W.; Schindelin, J.E.; Cardona, A.; Seung, H.S. Trainable Weka Segmentation: A machine learning tool for microscopy pixel classification. *Bioinformatics* **2017**, *33*, 2424–2426. [CrossRef] [PubMed]

53. Rueden, C.T.; Schindelin, J.; Hiner, M.C.; Dezonia, B.E.; Walter, A.E.; Arena, E.T.; Eliceiri, K.W. ImageJ2: ImageJ for the next generation of scientific image data. *BMC Bioinform.* **2017**, *18*, 529. [CrossRef] [PubMed]